INSTITUTE OF PHYSICS PUBLISHING NANOTECHNOLOGY
Nanotechnology **17** (2006) 3400–3411 doi:10.1088/0957-4484/17/14/010

Spatial resolution, information limit, and contrast transfer in piezoresponse force microscopy

S V Kalinin[1], **S Jesse, B J Rodriguez, J Shin, A P Baddorf, H N Lee, A Borisevich and S J Pennycook**

Materials Science and Technology Division, Oak Ridge National Laboratory, Oak Ridge, TN 37831, USA

E-mail: sergei2@ornl.gov

Received 17 November 2005, in final form 9 May 2006
Published 15 June 2006
Online at stacks.iop.org/Nano/17/3400

Abstract
Scanning probe-based ferroelectric domain imaging and patterning has attracted broad attention for use in the characterization of ferroelectric materials, ultrahigh density data storage, and nanofabrication. The viability of these applications is limited by the minimal domain size that can be fabricated and reliably detected by scanning probe microscopy. Here, the contrast transfer mechanism in piezoresponse force microscopy (PFM) of ferroelectric materials is analysed in detail. A consistent definition of resolution is developed both for the writing and the imaging processes, and the concept of an information limit in PFM is established. Experimental determination of the object transfer function and the subsequent reconstruction of an 'ideal image' is demonstrated. This contrast transfer theory provides a quantitative basis for image interpretation and allows for the comparison of different instruments in PFM. It is shown that experimentally observed domain sizes can be limited by the resolution of the scanning probe microscope to the order of tens of nanometres even though smaller domains, of the order of several nanometres, can be created.

(Some figures in this article are in colour only in the electronic version)

1. Introduction

In the decade since its invention [1, 2], piezoresponse force microscopy (PFM) has become the primary tool for imaging, spectroscopy, and manipulation of ferroelectric materials on the nanoscale [3, 4]. Of particular interest are applications of PFM for high resolution imaging of nanoscale piezoelectric materials including ferroelectric nanocrystals [5] and thin films [6], characterization of biological systems such as calcified and connective tissues [7, 8], and nanoscale domain patterning for data storage [9] and ferroelectric lithography [10].

The unique feature of PFM is that the scanning probe microscope (SPM) tip can be used both to *write* a domain structure by applying a predefined dc voltage to the tip inducing a local polarization reorientation in ferroelectric materials, and subsequently to *read* the resulting domain structure. Due to the fact that a ferroelectric domain wall is extremely narrow (one to two unit cells), domains of the order of nanometres can be created. Therefore, PFM techniques have been proposed as a basis for ferroelectric data storage. Originally, most of the effort was concentrated on fabricating a single domain with the smallest possible size. Depending on the material, domains with diameters of 150 nm [11], 80 nm [12], 40 nm [13, 14], and 20 nm [15] have been fabricated and imaged. Notably, a 20 nm bit size corresponds to a data storage density of roughly 2 Tb in $^{-2}$. However, a determination of the minimal domain size from a single-domain writing experiment is subject to several uncertainties related to the electrostatic offsets in the signal and to unreliable identification of the domain against the background noise. Moreover, practical data storage applications necessitate the creation of discrete ferroelectric bit arrays in which the

[1] Author to whom any correspondence should be addressed.

interaction of neighbouring domains is forbidden. The reported bit sizes in domain arrays are 360 nm [12], 94 nm [13], 66 nm [15], and 27 nm [16] when PFM is used to write and to read the domain arrays.

While PFM is considered the primary tool for ferroelectric characterization on the nanoscale, other SPM techniques have also been employed for that purpose. In particular, scanning nonlinear dielectric microscopy (SNDM) [17], based on purely electrical detection, has been used to write and read domains as small as 5 nm—the smallest domain size reported to date [18]. The smallest bit in an array as read by SNDM is 8 nm [19].

These applications require a quantitative assessment of the ferroelectric domain structure that can only be accomplished when the SPM image formation mechanism is well understood. In particular, further progress in the field requires a consistent definition of the *spatial resolution* to be established. This would enable comparisons of results obtained by different groups and on different experimental set-ups, allow the fidelity of PFM data storage and ferroelectric lithography to be determined, and unambiguously analyse statistical characteristics of domains, domain wall geometries, and domain distributions. Ultimately, quantitative knowledge of the image formation mechanism allows material properties and probe effects to be deconvoluted using a transfer function approach. The definitions developed in this work are applicable to any scanning probe technique provided that the signal is linear with respect to materials properties.

2. PFM principles and theory

In PFM, a conductive tip, biased with $V_{\text{tip}} = V_{\text{dc}} + V_{\text{ac}}\cos(\omega t)$, is brought into contact with the surface and the electromechanical response of the surface is detected as the first harmonic component of bias-induced tip deflection, $d = d_0 + d_{1\omega}\cos(\omega t + \varphi)$ [3, 4]. The phase of the electromechanical response, φ, yields information on the polarization direction below the tip. For c^- domains (polarization vector pointing into the surface) the application of a positive tip bias results in the expansion of the sample and surface oscillations are in phase with the tip voltage, $\varphi = 0$. For c^+ domains, $\varphi = 180°$. Experimentally, the phase shift between antiparallel domains can be less than 180° due to the presence of an electrostatic offset or cross-talk inevitable at high (500 kHz–5 MHz) imaging frequencies. The phase shift between antiparallel domains thus provides a necessary (but not sufficient) criterion for the veracity of the electromechanical signal. Traditionally, the PFM signal is plotted either as a pair of amplitude–phase, $A = d_{1\omega}/V_{\text{ac}}$, φ, images or as a mixed signal representation in which the piezoresponse, $\text{PR} = A\cos\varphi$, is mapped. Hence, in PFM, the resolution can be defined for either the mixed signal, PR, or phase, φ, images. Here, we discuss the resolution theory for the mixed signal and analyse the implications of using the phase signal to determine resolution.

The resolution and probed volume in PFM is determined by the structure of the electroelastic fields inside the material, or more precisely as the voltage derivative of the normal displacement field, $\partial u_3(\mathbf{x})/\partial V$. In general, a calculation of the electroelastic fields in the material requires the solution to a coupled problem, which is currently available only for a transversally isotropic case. Moreover, electric field generated outside the contact area is neglected [19, 20]. A simplified approach suggested by Felten [21] and Gopalan [22] is based on solving a decoupled problem. In this case: (a) the electric field in the material is calculated using a rigid electrostatic model (no piezoelectric coupling), (b) the strain or stress field is calculated using constitutive relations for a piezoelectric solid, and (c) the displacement field is evaluated using an appropriate Green's function for an isotropic or anisotropic solid. Here we analyse the validity of this approach and develop a general framework for contrast formation in PFM.

For linear piezoelectric materials, the relationship between strain, displacement, and field is

$$x_i = s_{ij}X_j + d_{ik}E_k \tag{1}$$

$$D_i = d_{ij}X_j + \varepsilon_{ik}E_k, \tag{2}$$

where x_i and X_j are the components of strain and stress tensors, D_i and E_k are the components of electric displacement and electric field vectors, d_{ij}, s_{ij} and ε_{ik} are components of piezoelectric constant, elastic compliance, and dielectric constant tensors in reduced Voigt notation.

The relative contributions of the different terms in equations (1) and (2) are estimated using a simple model. For a contact radius of ∼5 nm, corresponding to an indentation force of ∼100 nN and a tip radius of curvature of 50 nm, the average stress below the tip is 1.27 GPa. The electric field generated by a tip bias of 10 V is 2×10^9 V m^{-1}. For a typical elastic compliance of the order of 10^{-11} m^2 N^{-1} and a piezoelectric constant equal to 50 pm V^{-1}, the first term in equation (1) is 0.013 and the second is 0.1. In equation (2), assuming the direct effect and a dielectric constant of 100, the first term is 0.064 and the second is 1.77. From this estimate, the dielectric term dominates equation (2), thus justifying the use of the rigid dielectric approximation for calculating the electric field in the material. This analysis is corroborated by the exact solution for a transversally isotropic material [19]. Moreover, it was found that the contribution of the piezoelectric constants to the effective elastic properties is small and generally does not exceed 10–20%.

Using the Green's function theory suggested by Felten *et al* [21] the vertical surface displacement at the position of the tip, $u_3(\mathbf{y})$, can be written as

$$u_3(\mathbf{y}) = \int_{x_3=0}^{\infty}\int_{x_2=-\infty}^{\infty}\int_{x_1=-\infty}^{\infty} c_{jlmn}d_{mnk}\left(\mathbf{x}'\right)E_k\left(\mathbf{x}'-\mathbf{y}\right) \times \frac{\partial}{\partial x_l'}G_{3j}\left(\mathbf{y},\mathbf{x}'\right)\mathrm{d}\mathbf{x}' \tag{3}$$

where $\mathbf{x}'$ is the coordinate system related to the material, d_{mnk} are the piezoelectric coefficients and c_{jlmn} are the components of the elastic stiffness tensor. $E_k(\mathbf{x}'-\mathbf{y})$ is the electric field strength distribution produced by the probe. The Green's function for a semi-infinite medium $G_{3j}(\mathbf{y},\mathbf{x}')$ links the eigenstrains $c_{jlmn}d_{mnk}E_k$ to the displacement field. Equation (3) is significantly simplified if $c_{jlmn}d_{mnk}(y-\mathbf{x}'',z) = c_{jlmn}d_{mnk}(y-\mathbf{x}'')$, i.e. the system is uniform in the z-direction as in the case of a system with 180° domain walls normal to the surface. In this case, equation (4) can be rewritten as

$$u_3(\mathbf{y}) = -\int_S c_{jlmn}d_{mnk}\left(y-\mathbf{x}''\right)\left(\int_{z=0}^{\infty}E_k\left(-\mathbf{x}'',z\right) \times \frac{\partial}{\partial x_l'}G_{3j}\left(x'',z\right)\mathrm{d}z\right)\mathrm{d}S, \tag{4}$$

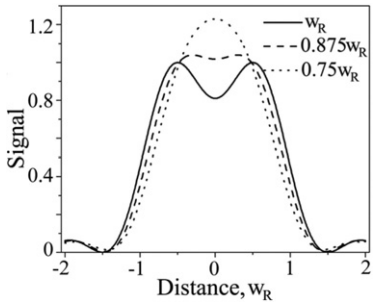

Figure 1. Rayleigh's definition of resolution. Solid, dash and dotted lines correspond to the different separation between scatterers.

that is, a convolution of a function describing the spatial distribution of material properties (left term) and a function related to probe parameters (right term). This representation for the PFM contrast is valid if the piezoelectric and dielectric properties do not change in the z-direction on the length scale of the field penetration depth.

The form of equation (4), where the material (sample) parameters and the instrument (probe) parameters are separated into different terms in a simple convolution, is not unique to PFM and also applies to magnetic force microscopy [23, 24] and Kelvin probe force microscopy [25, 26]. For such cases, the contrast formation mechanism can be analysed using transfer function theory that allows the definitions of resolution and information limit to be established, as discussed in detail below.

3. The resolution and information limit

The definition of spatial resolution originally evolved in the context of optical and electron microscopy. These techniques are ultimately based on optical or electron diffraction phenomena where the probed area is larger than or comparable to the wavelength, thus differing fundamentally from the near-field principle employed in most SPMs where the probed area is much smaller than the wavelength. Here, we briefly discuss resolution theory in classical optical and electron microscopy and analyse how these concepts can be applied to PFM.

The most traditional definition of resolution comes from light optics—the well-known Rayleigh criterion [27]. In this, resolution is defined as the minimum distance by which two point scatterers must be separated to be discernible for a given wavelength and aperture of the imaging system. A commonly used alternative reading of the criterion postulates that for two Gaussian-shaped image features of similar intensity to be resolved, the dip between the two maxima should be at least 21% of the maximum. This criterion is illustrated in figure 1 and shows the transition of the two features from completely resolved to unresolved as a function of the separation distance. Note that the criterion is not absolute. It is possible that, for a system with a sufficiently high signal-to-noise ratio, peaks separated by less than the Rayleigh resolution can be discernible (for example, the dashed line on figure 1), or that a system with a low signal-to-noise ratio will require larger separations. Another important limitation is connected to the fact that this criterion was derived for the incoherent (phase independent) imaging conditions and thus is not extendable to all microscopic techniques, notably to phase contrast transmission electron microscopy (TEM) [28, 29]. Thus for TEM, an alternative approach was developed based on *contrast transfer functions* (CTFs), which are determined by microscope parameters such as defocus and lens aberrations [30].

The CTF is a reciprocal space function that describes the sign and fractional transfer of spatial frequencies from the object to the image. Solids at high magnification (TEM samples) have a discrete spectrum of spatial frequencies q, corresponding to interatomic spacings d, where $q = 1/d$. The CTF is defined for an idealized 'weak phase object', which is realized in practice by thin amorphous samples or very thin crystalline samples. In this case, the TEM image intensity can be written in terms of the spatial frequency [29]:

$$I_L(\mathbf{q}) = \delta(\mathbf{q}) + O(\mathbf{q}) \times F(\mathbf{q}) = \delta(\mathbf{q}) + O(\mathbf{q}) \times \sin\chi(\mathbf{q}) \times E_\Delta(\mathbf{q}) \times E_\alpha(\mathbf{q}), \quad (5)$$

where $O(\mathbf{q})$ is the object or sample function, and $F(q)$ is the CTF, which consists of the aberration-dependent $\sin\chi(\mathbf{q})$ [30] and two damping envelope functions: $E_\Delta(\mathbf{q})$, accounting for the spread of the focus, and $E_\alpha(\mathbf{q})$, accounting for the beam convergence [31]. The envelope functions attenuate transfer at high spatial frequencies.

The shape of the TEM CTF can be very complicated (figure 2(a))—it is non-monotonic and exhibits multiple maxima and contrast reversals. Additionally, the shape can be changed by varying the defocus. Imaging conditions are usually adjusted in order to extend the range of spatial frequencies where the CTF is fairly large and varies slowly, thus facilitating direct image interpretation [30, 29]. Under these conditions (Sherzer defocus) the spatial frequency where the CTF first crosses zero is referred to as the point

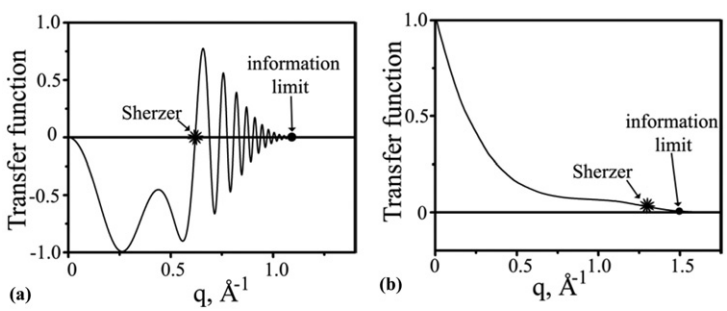

Figure 2. Typical contrast transfer function in (a) phase contrast transmission electron microscopy and (b) scanning transmission electron microscopy. The characteristic oscillations in (a) are due to coherence.

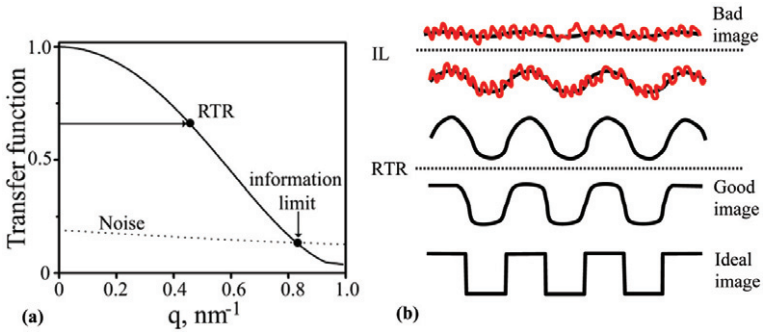

Figure 3. (a) Anticipated CTF in near-field SPM and (b) evolution of ideal image with decreasing resolution. The dotted lines correspond to the Rayleigh two-point resolution limit and the information limit (IL).

(or Scherzer) resolution. The spatial frequency beyond which there is no information transfer is the information limit. Note that as the lens aberrations are corrected, the point resolution of the phase contrast imaging is extended towards the information limit [32].

The situation is greatly simplified for Z-contrast scanning transmission electron microscopy (STEM). In Z-contrast STEM, the signal on a high angle annular dark field detector is integrated over a large angular range, resulting in an incoherent image [33, 34]. Thus Z-contrast STEM image intensity can be presented as a simple convolution:

$$I(\mathbf{x}) = \int O(\mathbf{x}-\mathbf{y})F(\mathbf{y})\mathrm{d}\mathbf{y} = \int O(\mathbf{x}-\mathbf{y})P^2(\mathbf{y})\mathrm{d}\mathbf{y} \quad (6)$$

i.e. the resolution function $F(\mathbf{x})$ is in fact the probe intensity, $P^2(\mathbf{x})$. In reciprocal space, equation (6) becomes

$$I(\mathbf{q}) = \mathbf{O}(\mathbf{q})T(\mathbf{q}), \quad (7)$$

where $T(\mathbf{q})$ is the STEM transfer function, which is the Fourier transform of the probe intensity. Unlike the phase contrast CTF (see figure 2(a)), the STEM transfer function $T(\mathbf{q})$ is always positive in the absence of aberrations, although it still depends on the defocus. The Sherzer resolution [30] and information limit can also be defined for this imaging mode (figure 2(b)). In STEM an observation of visibly separated atomic columns corresponding to a known crystallographic spacing (a Rayleigh-like criterion) is considered an unequivocal proof of the resolution of that numerical value [35]. The Fourier transform of the image intensity is referred to as a diffractogram. The highest spatial frequency present in the diffractogram represents an information limit in a manner similar to the phase contrast definition.

Image formation described by equations such as (5) and (7), where the image intensity is given by a convolution of the object (sample) function and a resolution function, is often referred to as linear imaging. To generalize, the measured image $I(\mathbf{x})$, where $\mathbf{x}$ is a set of spatial coordinates, is given by the convolution of an *ideal image* (representing material properties) $I_0(\mathbf{x}-\mathbf{y})$ with the resolution function, $F(\mathbf{y})$:

$$I(\mathbf{x}) = \int I_0(\mathbf{x}-\mathbf{y})F(\mathbf{y})\,\mathrm{d}\mathbf{y} + N(\mathbf{x}) \quad (8)$$

where $N(\mathbf{x})$ is the noise function. The Fourier transform of equation (8) is

$$I(\mathbf{q}) = I_0(\mathbf{q})F(\mathbf{q}) + N(\mathbf{q}) \quad (9)$$

where $I(\mathbf{q}) = \int I(\mathbf{x})\mathrm{e}^{\mathrm{i}\mathbf{q}\mathbf{x}}\,\mathrm{d}\mathbf{x}$, $I_0(\mathbf{q})$, and $N(\mathbf{q})$ are the Fourier transforms of the measured image, ideal image, and noise, respectively. The object transfer function (OTF), $F(\mathbf{q})$, is defined as a Fourier transform of the resolution function, $F(\mathbf{y})$. The object transfer function, $F(\mathbf{q})$, and the resolution function, $F(\mathbf{y})$, can then be determined directly provided that the ideal image, $I_0(\mathbf{q})$, is known. Then, once the resolution function is determined for a known calibration standard, it can be used to extract the ideal image, $I_0(\mathbf{x})$, from a measured image, $I(\mathbf{x})$, for an arbitrary sample. In both phase contrast TEM and STEM, the ideal image can be calculated using known atomic positions and scattering cross-sections, thus significantly simplifying image interpretation.

Note that the form of equation (4), where the material (sample) parameters and the instrument (probe) parameters are separated into different terms of a simple convolution, corresponds to the linear theory described by equations (8) and (9). Notably, the *ideal image* in PFM is the distribution of strain piezoelectric constants $e_{ijk} = c_{jlmn}d_{mnk}$ that correlate with the domain structure of the material. The resolution function $F(\mathbf{y})$ in the form given by equation (5) depends on the electrostatic field generated by the tip. As such, it depends on tip geometry and contact conditions etc, and its calculation from the geometric parameters of the tip is subject to multiple uncertainties. Due to the linear form of equation (4), however, it can also be determined experimentally from a well-defined calibration standard. Moreover, the general behaviour of the resolution function in PFM can be analysed from simple physical arguments.

The image formation mechanism in PFM is ultimately based on the near-field interactions between the tip and the ferroelectric material, where the contact area is significantly smaller than the acoustic wavelength at the imaging frequency. Hence, the resolution function can be expected to be a monotonically decreasing function of distance and is not expected to have zeroes. For long distances, corresponding to point charge/force type models, power-law behaviour consistent with the typical behaviour of Green's functions in electroelastic problems is anticipated. Similar reasoning applies to the object transfer function. In Fourier space, an exponential decay for large wavevectors can be predicted from the finiteness of the field in the excited volume. The resulting generic form of the transfer function in PFM is shown in figure 3(a).

For the PFM OTF shown in figure 3(a), two definitions of resolution, analogous with those for HRTEM and

Z-STEM cases, can be formulated. The first definition can be derived from the Rayleigh criterion as the minimum separation between two point objects that can still be resolved by PFM [36]. This Rayleigh two-point resolution (RTR) establishes a conservative definition of resolution because even at this spacing a substantial change in contrast is still measurable between the two objects. However, unlike the HRTEM or Z-STEM situations, where CTF or OTF falls to zero at some spatial frequency, there are no natural zeroes in the PFM OTF. Therefore we use an alternative definition, the information limit, to define the minimum feature size that can still be detected in the presence of noise, as illustrated in figure 3(b).

For a material that is inhomogeneous in the z-direction, equation (3) has a significantly more complex structure than equation (4)—in particular, $G_{3j}(\mathbf{y}, \mathbf{x}')$ cannot be represented as $G_{3j}(\mathbf{y} - \mathbf{x}')$. Thus, in the general case of a non-uniform field distribution, the PFM image cannot be represented as a 2D convolution and, in the absence of information on domain wall orientations, etc, the change of materials properties in the z-direction cannot be addressed. Moreover, for topographically inhomogeneous surfaces the imaging mechanism becomes non-linear. This is similar to the situation for topographic AFM imaging [37]. In such cases, however, it may still be possible to analyse the spatial frequencies revealed in the image through a diffractogram provided that the features are real, as suggested by Engel [38] and Gutierrez [39].

4. Experimental details

PFM studies were carried out on a commercial SPM system (Veeco MultiMode NS-IIIA) equipped with additional function generators and lock-in amplifiers (DS 345 and SRS 830, Stanford Research Instruments, and model 7280, Signal Recovery). A custom-built sample holder was used to allow direct tip biasing and to minimize capacitive cross-talk with the SPM electronics. Measurements were performed using Au-coated Si tips (Micromasch, spring constant $k \sim 1$ N m^{-1}) typically at 500 kHz. The typical scan rate was 1 Hz, corresponding to a ~4 ms residence time for a single pixel. The time constant of the lock-in amplifier was systematically varied from 0.5 to 20 ms to establish its effect on the image.

Measurements were performed on pulsed-laser deposition grown 13 nm thick lead-titanate-zirconate (PZT) thin films on a $SrRuO_3$ electrode using metal-coated cantilevers (Cr–Au, Micromasch, $l \approx 130$ μm, resonant frequency ~150 kHz, spring constant $k \sim 4.5$ N m^{-1}). Standard calibration patterns were written using custom designed LabView/MatLab software. To determine the relationship between domain wall widths in phase and mixed signal images, a periodically poled $LiNbO_3$ (PPLN) sample was used.

5. Results and discussion

5.1. Determination of the information limit

To determine the OTF and information limit in PFM, we adopt an approach developed for STEM based on the analysis of the diffractograms of periodic structures. Periodic domain structures can either be created by writing or occur naturally, as in lamellar a–c domains of tetragonal ferroelectrics. Figure 4(a) shows the template pattern used to write domains on the PZT surface along with the corresponding diffractogram. Note that 'domain walls' in the writing pattern are extremely sharp. Hence, many (hk) peaks can be seen on the FT. For this symmetric lattice, the extinction rule is $h - k = 2n + 1$ $(n = 0, 1, \ldots)$. For comparison, shown in figures 4(c) and (d) are the resultant domain patterns imaged by PFM and their Fourier transforms. Note that only a few low order reflections can be observed in the diffractogram. Also, peaks that did not exist in the FT of the template pattern are visible in the read pattern (arrow). This effect is due to the fact that the relative areas occupied by the 'white' and 'black' domains are different on the written image as compared to the read image due to the significant imprint of ~1–2 V in the film. Thus, the voltage pattern used to create the domain structure does not rigorously represent the polarization distribution created in the film. The intensity of the 'forbidden' components can thus be used as a criterion for the fidelity of the writing procedure. The width of the peaks in the FT is a measure of the disorder associated with domain wall roughness and deviation in domain wall positions from ideal.

The contribution of the lock-in amplifier, which is used to extract the weak first harmonic signal from the tip oscillation signal, merits separate consideration. The effect of the lock-in time constant on PFM is illustrated in figures 4(b)–(f). Imaging with a low time constant (0.5 ms) results in a sharp, but relatively noisy, image (as seen in both the real-space and FT images). On increasing the time constant to 1 ms, the noise level decreases. However, increasing the time constant further, to 4, 10, and 20 ms, results in characteristic streaking in real-space images along the fast scan direction. Note the evolution of the noise background in the corresponding diffractograms from a rotationally isotropic noise pattern for small time constants (figures 4(b) and (c)) to a pronounced noise band in figures 4(d)–(f), indicating a large anisotropy of noise in the slow and fast scan directions. Also note that despite the high smearing in figure 4(f) from the large time constant (the pattern is not discernible in the real-space image), the corresponding diffractogram still contains reflections corresponding to the written pattern.

Figure 5(a) shows the wavevector dependence of the peak intensity of several (hk) reflections for different lock-in time constants. The peak intensities follow an exponential decay law, $I(hk) = I_0 \exp(-q/G)$, where the decay constant is independent of the lock-in settings, $G \approx 0.005$ nm^{-1}, $q = \sqrt{h^2 + k^2}/a$, and a is the periodicity of the lattice. Thus, the intensity of the (10) peak can be used as a measure of the overall peak to noise ratio of the diffractogram, and hence of the image quality. To determine the optimal imaging parameters, a plot of the intensity of the (10) peak as a function of lock-in settings is given in figure 5(b). The peak intensity is virtually constant for small lock-in time constants. However, it rapidly becomes zero when the time constant becomes larger than the time corresponding to the pixel acquisition rate (5 ms), in agreement with the qualitative results in figure 4.

From the data in figures 4 and 5 we propose that the actual PFM transfer function can be represented as $F(\mathbf{q}) = F_{\text{tip}}(q)F_{la}(q_x)$, where $F_{\text{tip}}(q)$ is the tip transfer function described by equation (4) and is assumed to be rotationally

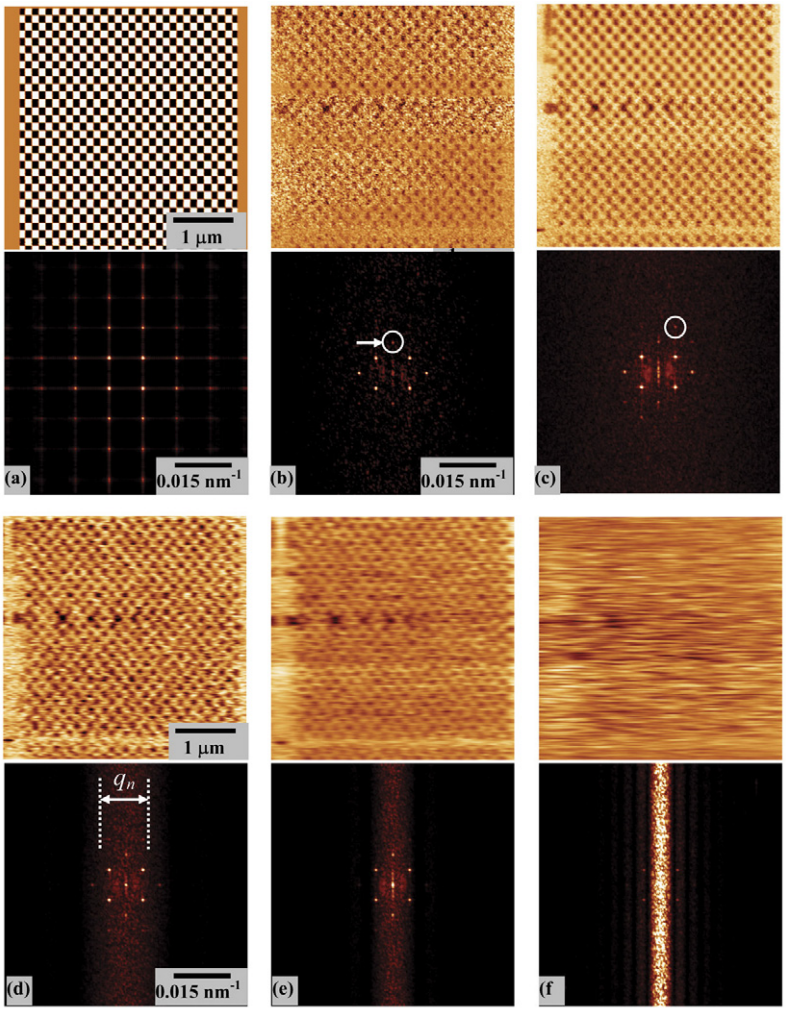

Figure 4. (a) Ideal image (writing signal) (top) and corresponding FFT image (bottom) illustrating that all frequency components are present. PFM images (top) and diffractograms (bottom) acquired with (b) 0.5 ms, (c) 1 ms, (d) 5 ms, (e) 10 ms, and (f) 20 ms lock-in time constants.

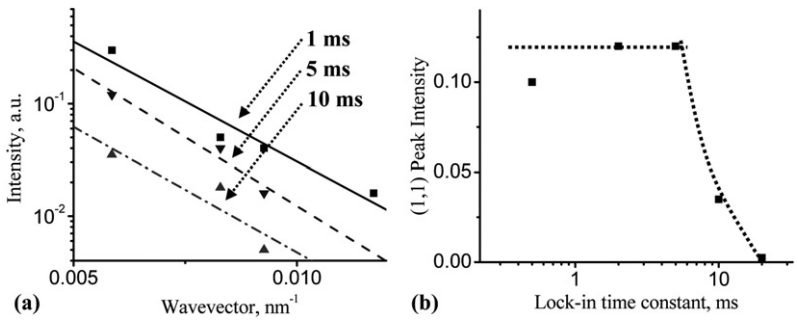

Figure 5. (a) Wavevector dependence of peak intensity for time constant (■) 1 ms, (▼) 10 ms, and (▲) 5 ms. (b) Intensity of the (1, 1) peak as a function of lock-in time constant.

invariant. $F_{la}(q_x)$ is the lock-in transfer function, where q_x is the wavevector corresponding to the fast scan axis. Note that the dependence on slow scan axis would only be important for time constants comparable to the line acquisition time—a situation incompatible with imaging. The lock-in transfer function depends both on the spatial coordinate and the residence time in each pixel and, in turn, determines the noise level in an image. In particular, for a lock-in time constant $\tau \ll \tau_{\text{pixel}}$ the $F_{la}(q_x) = 1$. The noise intensity in this case is almost uniform, $N(\mathbf{q}) \approx N(q)$ and, for white noise, scales with the time constant as $N(q) \sim \sqrt{\tau_{\text{pixel}}/\tau}$.[2] The noise decreases for large time constants. However, for $\tau > \tau_{\text{pixel}}$ the lock-in causes 'smearing' of the image in the x-direction (streaks) and the noise spectral density acquires a

[2] Noise in the slow scan axis direction can be anticipated to be higher due to drift, etc.

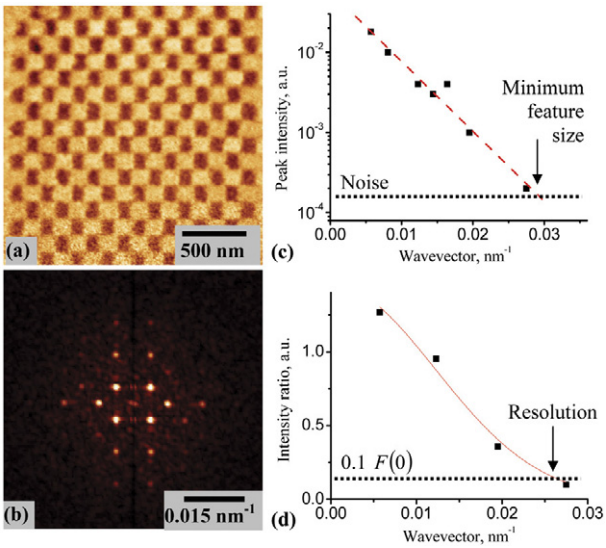

Figure 6. (a) PFM image of a grid pattern and (b) corresponding FFT image. (c) Wavevector dependence of the FFT peak intensity illustrating the minimal feature size. (d) Calculated transfer function illustrating resolution.

profound anisotropy. The characteristic width of the noise band in figures 4(b), (d), and (f) scales as $q_n \sim q_{\max}\tau_{\text{pixel}}/\tau$, where $q_{\max}$ is the maximum frequency in the image[3]. The image quality can be significantly improved, i.e. the noise level can be decreased, by imaging at slower scan rates, that is, higher τ_{pixel}. Slower scanning generally allows higher-quality images to be obtained at the expense of an increased acquisition time. However, this approach is ultimately limited by the thermal drift of the microscope and the eventual dominance of $1/f$ noise.

To determine the resolution function, $F(\mathbf{y})$, we utilize the approach adopted in electron microscopy based on equation (9). Shown in figure 6(a) is a 2 μm image (acquired with a different probe from that used to figure 4) along with the corresponding diffractogram, figure 6(b). The wavevector dependence of the peak intensities is shown in figure 6(c), where $I(hk) = I_0 \exp(-q/G)$ with $G \approx 0.011$ nm^{-1}. The information limit is determined by the condition $I(hk) = N(q)$ and, from figure 6(c), it is estimated to be 33 nm. The ratio of the experimental to the ideal diffractogram intensities is shown in figure 6(d), which from equation (7) defines the OTF. The transfer function can be approximated by the Gaussian form

$$F(q) = A\exp\left(-q^2/2w^2\right), \tag{10}$$

where $A = (1.45 \pm 0.08) \times 10^{-3}$ and $w = (12.2 \pm 0.8) \times 10^{-3}$ nm^{-1}, as shown by the solid line in the figure. The PFM resolution function in real space can then be readily found by inverse Fourier transform as

$$F(r) = 2Aw\exp\left(-w^2r^2/2\right). \tag{11}$$

To determine the Rayleigh two-point resolution from the resolution function, we map the transfer function theory onto the Rayleigh approach. For an ideal image formed by two δ-function type point sources, equation (8) yields

$$I(\mathbf{x}) = F\left(-x'\right) + F\left(x'\right). \tag{12}$$

Thus, for a known OTF in Fourier space, $F(q)$, the resolution function in real space, $F(x)$, can be reconstructed, and equation (14) can be used to relate the transfer function to the resolution as defined by the Rayleigh criterion, w_{R}, as $F(w_{\text{R}})/F(0) = 0.58$. For the Gaussian resolution function in equation (11), the condition $F(w_{\text{R}})/F(0) = 0.58$ is equivalent to $w_{\text{R}} = 1/w$ and for the data in figure 6 the Rayleigh resolution is therefore $w_{\text{R}} = 82$ nm.

Note that the resolution and contrast transfer function above are defined assuming the writing pattern is the ideal image. Hence, the RTR in this case defines the minimal domain size that can be reliably written for the given probe, material, and writing conditions. Moreover, these quantities, which are related to the periodicity of the structure, represent an average resolution for the whole image. Hence, the OTF and RTR are sensitive to the deviations of the domain shape from the ideal, signal variations within the domain due to surface imperfections or contamination, etc. These definitions provide a quantitative measure of the information transfer from the desired template pattern to the actual image of the resulting domain structure, and so describe the fidelity of ferroelectric data storage rather than reading resolution *per se*.

However, it is often necessary to define the resolution in existing domain structures in ferroelectric and piezoelectric materials. In this case, the ideal image is typically not known. Moreover, naturally forming periodic domain patterns are rare. Hence, to define a pure reading resolution for PFM, we relate the resolution and transfer functions to the domain wall widths to be determined locally, as described below.

5.2. The determination of PFM resolution from real-space images

The PFM resolution in real space can be simply determined from the measured width of the domain wall between antiparallel domains[4]. Given that the intrinsic width of a ferroelectric domain wall is of the order of one to two unit cells (~1 nm) [40], the typical effective domain wall width observed in PFM is currently of the order of 5–50 nm and therefore reflects primarily the spatial resolution of the microscope. In particular, due to the symmetry properties of the dielectric, elastic, and piezoelectric constant tensors, the piezoelectric constants change sign across a 180° domain wall, while the elastic and dielectric properties do not. Hence, the relationship between the 180° domain wall width and the resolution function can be established from equation (5), where, after normalization, the domain wall profile is given by

$$\text{PR}(x) = \int_{-\infty}^{x} \text{d}x' \int_{-\infty}^{\infty} F\left(x', y\right) \text{d}y - \int_{x}^{\infty} \text{d}x' \times \int_{-\infty}^{\infty} F\left(x', y\right) \text{d}y + N(\mathbf{x}). \tag{13}$$

Experimentally, the width of the domain wall image can be determined from the derivative at the centre, x_0, as

[3] The image can be significantly improved if the lock-in is synchronized with the pixel acquisition time.

[4] For non-180° domain walls, strain can result in additional domain wall broadening.

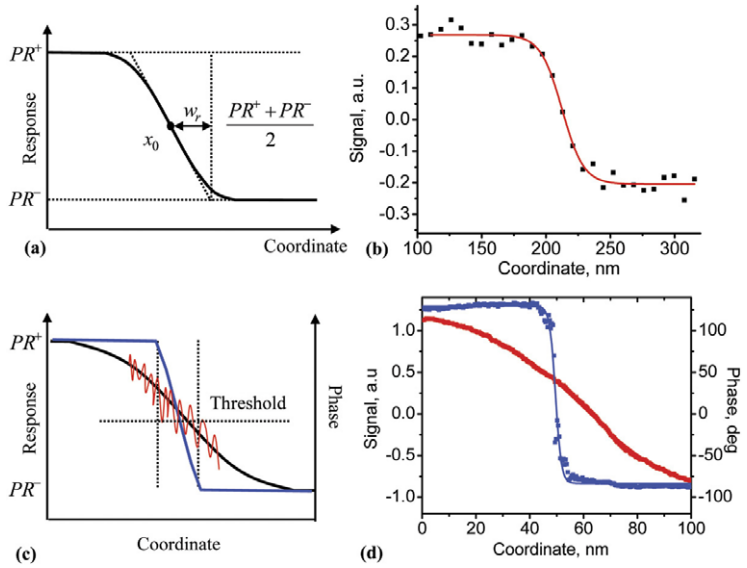

Figure 7. (a) Schematics of the domain wall profile and definition of domain wall width. (b) Domain wall profile through one of the walls in figure 6(a) and fit by equation (14). (c) Relationship between domain wall width and resolution in mixed signal and phase images. (d) Amplitude (red/thick solid line) and phase (blue/dotted solid line) profiles across the domain wall in periodically poled $LiNbO_3$.

$w_r = (\mathrm{PR}^+ + \mathrm{PR}^-)/2\mathrm{PR}'(x_0)$ (figure 7(a)). This definition can also be used if the domain wall profile is fitted using a suitable function (e.g. a phenomenological function such as the Boltzmann sigma function, or reflecting the polarization profile across a domain wall in the mean field theory). For example, with a Boltzmann fit, $\mathrm{PR}(x) = \mathrm{PR}^- + (\mathrm{PR}^+ - \mathrm{PR}^-)/(1 + \exp[(x - x_0)/x_\mathrm{d}])$, the domain wall image width is $w_r = 2x_\mathrm{d}$. Note that the signal gradient at the domain wall provides an upper limit of the 'sharpness' of any intrinsic feature in the image.

The domain wall width (corresponding to edge resolution in optical microscopy) can be naturally related to the Rayleigh resolution defined in section 5.1. For the resolution function given by equation (11), the domain wall profile is given (after normalization) by

$$\mathrm{PR}(x) = \frac{1}{2}\left(1 + \mathrm{Erf}\left(\frac{wx}{\sqrt{2}}\right)\right). \qquad (14)$$

From equation (14), the domain wall width is related to the OTF parameters as $w_\mathrm{d} = \sqrt{\pi/2}/(2w)$ and for the experimental data in figure 6 is found to be $w_\mathrm{d} = 51.3$ nm. For a Gaussian OTF, the relationship between domain wall width and Rayleigh resolution is $w_\mathrm{d} = 0.626 w_\mathrm{R}$.

Shown in figure 7(b) are PFM signals across a typical domain wall in figure 6(a). The domain wall width, determined from the fit to equation (14), is $w_\mathrm{dr} = 16$ nm. This significant discrepancy between the domain wall width estimated from the OTF and this local measurement is due to the aforementioned differences between the writing–reading versus reading only processes as well as average versus local data. Understandably, a profile taken perpendicular to a domain wall is less affected by imperfections in the wall shape, and is not at all affected by imperfections in the shapes of the other domain walls. Hence, the domain wall width determined in reading process can be used as a quantitative measure of the spatial resolution of a given PFM image, while RTR determined from the diffractogram is a measure of the fidelity of the writing–reading process.

Note that in the derivation of equations (11) and (14) relating Rayleigh resolution and domain wall width to the OTF, we explicitly used the Gaussian approximation for the OTF. However, this functional form is phenomenological. The large-q behaviour of the OTF is difficult to determine due to noise effects, and thus limits the amount of information that can be obtained experimentally. Once an appropriate functional form for the OTF based on a known mechanism for the tip–surface interactions is available, analysis similar to equations (11) and (14) can be performed. However, given that the OTF in PFM has to be a rapidly decaying monotonic function of q (or x), a Gaussian should serve as a reasonable approximation. Hence the relationship between the Gaussian width, Rayleigh resolution, and the domain wall width obtained for Gaussian CTF can be expected to be a good approximation for other functional forms.

5.3. Resolution in phase images

One of the difficulties in defining the resolution in PFM stems from differences between the phase and mixed signal images (section 2). The relationship between the two is illustrated in figure 7(c). While the normalized PFM signal, pr, changes between -1 and 1, the phase signal for zero noise can adopt values of 0° for $pr < 0$ and 180° for $pr > 0$. In the presence of an offset due to electrostatic contributions to the PFM signal, capacitive cross-talk in cabling, etc, the phase changes at some critical value, pr_c. Thus, the phase image is similar to an image on which a thresholding operation has been performed. In the presence of noise, the evolution of a phase signal can be understood from the schematics in figure 7(c). The phase achieves limiting values when the mixed signal is either significantly larger or smaller than the characteristic

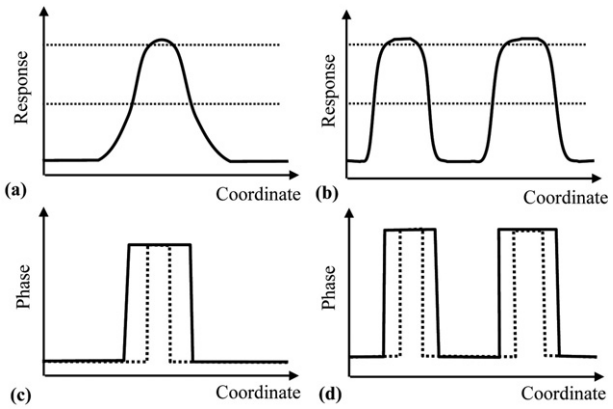

Figure 8. (a) Domain size on mixed-signal and phase PFM images. (b) The conversion of a mixed signal to a phase signal is similar to a thresholding operation, where the threshold is determined by the instrumental settings and the electrostatic contribution to the signal. For a threshold other then 0, the domain size can be significantly different from reality. Note that unlike a mixed signal, the signal strength in the phase image does not depend on domain size. (c), (d) For periodic domain size, the increase in the domain of one polarity is compensated by the decrease in the size of domains of the opposite polarity, providing a quantitative measure of minimal domain size.

noise amplitude and changes rapidly in the region where the noise amplitude is sufficiently large to place the signal above or below the threshold value. Hence, the width of the domain wall in the phase image can be estimated as $w_\varphi = \langle N\rangle/2\mathrm{PR}'(x_0)$, where $\langle N\rangle$ is the average noise amplitude. Hence, the resolution as measured from the phase image is higher than that in the mixed signal, $w_\varphi = w_\mathrm{d}(\mathrm{PR}^+ + \mathrm{PR}^-)/\langle N\rangle$, since the noise level is typically small compared to the signal. From the schematics in figure 7(c), we conclude that the effective Rayleigh resolution for the phase signal corresponds to the information limit of the mixed PFM signal.

Experimentally, the domain wall width determined from phase data is ∼0.5–1 orders of magnitude lower than that in the mixed signal, as illustrated by the PFM mixed-signal and phase data in figure 7(d). Given that the domain wall width in a mixed signal can be as small as 5–10 nm, the width in the phase image can be as small as a fraction of a nanometre. However, since the phase signal contains only a fraction of the information contained in the mixed PFM image and the thresholding operation is non-linear (hence linear theory equations (8) and (9) do not apply), the object transfer function and the true Rayleigh resolution and material properties cannot be determined from the phase data until a proper model of the tip–surface interactions is developed.

The possible effects of phase imaging on PFM data analysis are illustrated in figure 8. For a single written domain, variation of the thresholding level (using data processing or due to electrostatic contributions to the PFM signal) can result in a significant reduction of the effective domain size and ultimately to the size corresponding to the information limit of the technique. This is not the case for periodic domain structures, however, where a decrease of domain size of one polarity is compensated by an increase of domain size of the opposite polarity, thus maintaining the overall periodicity of the lattice.

5.4. The minimal detectable feature size in PFM

The effect of domain wall width on the detectable domain size is illustrated in figure 9(a). For domain sizes, r_d, larger than the domain wall width, the domains are readily detectable and the signal in the centre approaches the value for the infinite material, i.e. imaging is *quantitative*. However, for $r_\mathrm{d} < w_r$, the signal in the domain centre decreases rapidly with r. For small circular domains, the contrast in the centre measured relative to background can be readily found from equation (8) as

$$\mathrm{PR}(r_\mathrm{d}) = \mathrm{PR}_\mathrm{max}\int \theta\,(\mathbf{r}-\mathbf{r_d})F\,(\mathbf{r})\;\mathrm{d}\mathbf{r} \qquad (15)$$

where $\mathrm{PR}(r_\mathrm{d})$ is the response in the centre of the domain centred at the origin as a function of characteristic domain size

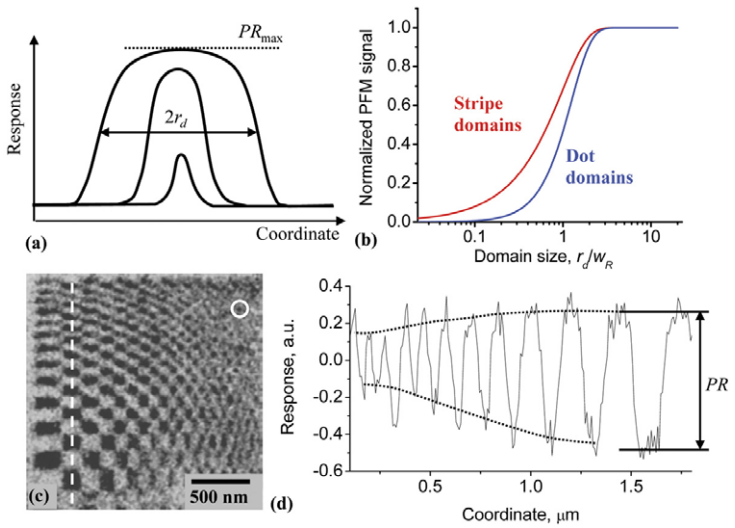

Figure 9. (a) Schematics of signal evolution with domain size for stripe or dot domains. (b) Calculated signal strength for stripe and dot domains for a Gaussian OTF. (c) PFM image of a variable sized grid test pattern consisting of multiple strip and dot domains. (d) Profile along the dotted line in (c), illustrating the resolution effect on signal and minimal feature size.

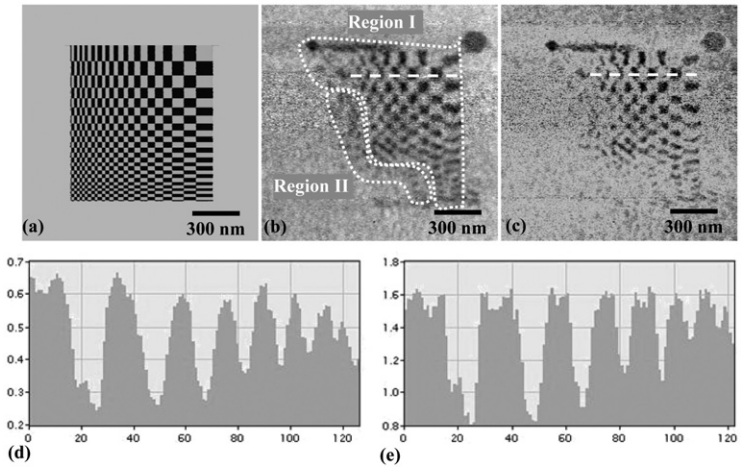

Figure 10. (a) Writing pattern, (b) original PFM image and (c) reconstructed PFM image using the transfer function. (d) Original and (e) reconstructed profiles along the dotted lines in (b) and (c). Notice the difference in domain wall width.

r_d and the Heaviside step function, $\theta(x)$, is 1 for $x \geqslant 0$ and $\theta(x) = 0$ for $x < 0$. The integration is taken over the area $\mathbf{r_d}$ within the domain. Note that in this case the presence of a domain can still be detected by PFM (if above the noise level), but the signal is no longer quantitative (i.e. the signal measured in the centre of the domain is size-dependent and is reduced compared to the signal in an infinite domain).

For the Gaussian OTF in equations (10) and (15), the domain contrast as a function of domain radius for a stripe domain of width r_d is

$$\mathrm{PR}(r_d) = \mathrm{Erf}\left(\frac{w r_d}{\sqrt{2}}\right). \tag{16}$$

The signal in the centre of the domain decreases to 80% of the saturation signal for $r_d = 1.282/w = 1.282 w_R$ (or, equivalently, $r_d = 0.80 w_d$) and to 20% of the saturation signal for $r_d = 0.25 w_R$ (or $r_d = 0.16 w_d$). For a square domain of size r_d, the signal in the centre is

$$\mathrm{PR}(r_d) = \left\{\mathrm{Erf}\left(\frac{w r_d}{\sqrt{2}}\right)\right\}^2. \tag{17}$$

In this case, the signal in the centre decreases to 80% of the saturation signal for $r_d = 1.618 w_R$ ($r_d = 1.01 w_d$) and to 20% of the saturation signal for $r_d = 0.594 w_R$ ($r_d = 0.37 w_d$). Thus, for domain sizes smaller than the resolution (or domain wall width), the maximum response signal decreases with domain size (linearly for stripe domains, quadratically for dots). This behaviour is illustrated in figure 9(b). This decrease is related to the finite resolution rather than to changes in the material properties, and hence this effect is important in the interpretation of the PFM signal from nanoscale objects (e.g. domains written by PFM or polar nanoregions in ferroelectric relaxors). However, note that the domain can be *detected* when its size is significantly below the resolution but still larger than the noise amplitude, i.e. at the information limit of the measurement.

For optimal lock-in settings, the real-space definition of minimal feature size is illustrated in figure 9(c), where the domain pattern is created using a variable size mesh that contains both stripe and square domains in the slow and fast scan directions. The profile along the dotted line is illustrated in figure 9(d). Note that the domain wall width is ∼30 nm, providing a measure of the resolution of the technique. For large domains, the signal saturates both on the top and bottom of the domain, while for smaller domains, the domain walls overlap, resulting in a characteristic triangular shape. However, the domain can still be detected. The domain contrast virtually disappears in the top right corner of the grid, defining the information limit to be of the order of ∼10–30 nm. Note that unambiguous determination of the information limit requires the use of a diffractogram as described section 5.1. The information limit, or *minimal detectable feature size* in this case is significantly smaller than the domain wall width (Rayleigh resolution).

5.5. Image reconstruction in PFM

Finally, the experimentally determined resolution function can be used to reconstruct an 'ideal image', as demonstrated in figure 10. The template pattern and corresponding domain pattern are shown in figures 10(a) and (b). For deconvolution, the recorded image diffractogram was divided by the transfer function. To avoid the spurious amplification of the large-q features, a noise offset of 0.1 $F(0)$ was introduced before the division. The resulting deconvoluted image is shown in figure 10(c). The reconstruction is successful only in Region I, where the domain size is above the information limit. Note the difference in the image contrast between the original and reconstructed images. This behaviour is further illustrated in figures 10(d) and (e) showing line profiles across the images in figures 10(b) and (c). Note the decrease in domain wall width indicative of an ideal image. Also note that the minimum domain size detected by PFM in this case is limited by the resolution of the technique, suggesting that the reading resolution is a limiting factor precluding experimental observation of smaller domains that can be written by PFM.

The quality of the deconvoluted images can be significantly improved through the use of probability-based iterative methods such as maximum entropy reconstruction [41, 42] or

Pixon reconstruction [43]. Both methods were shown to produce good results for Z-contrast STEM images [44, 45].

5.6. Writing in PFM

The implicit assumption used throughout this paper is that the template voltage pattern used for domain writing (figure 4(a)) and the written ferroelectric domain pattern are equivalent. In other words, the writing is assumed to be a binary process, in which the application of positive bias results in a positive domain, and a negative bias results in formation of a negative domain. As follows from the comparison of the diffractograms in figures 4(a)–(f), the written domain pattern actually deviates from the template. Note that the domain writing process is highly non-linear, and the size of the nascent domain is determined by the tip bias, geometry, and material [46, 47]. As shown by several authors [48–52], domain nucleation in PFM requires a certain critical bias to be achieved, above which the domain grows with bias. Hence, the writing voltage and resulting domain pattern cannot be related using simple linear theory as in equations (8) and (9).

Another interesting consequence of the domain nucleation mechanism in PFM is that the minimum writable domain size is not necessarily related to the information limit in PFM and can be either larger or smaller. This follows from the fact that while the signal generation volume in PFM is independent of the tip bias, the written domain size, and in particular the critical size of the nucleated domain, has a strong bias dependence, i.e. the minimum writable domain size can be smaller than the PFM resolution. In the case of the PZT film used in the present work, the minimum domain size detected by PFM is limited by the information limit of the technique, as follows from the fact that domains gradually disappear for short writing pulses in figures 9(c) and 10(b). This suggests that in this case the resolution is a limiting factor precluding experimental observation of smaller domains created by PFM. Such domains can be detected by the change in average PFM signal (Region II in figure 10(b)) [53]. Clearly, this conclusion is non-universal and strongly depends on the material, e.g. in polycrystalline films the grain by grain switching will result in minimal writable bit sizes being larger than the resolution.

6. Summary

To summarize, the contrast transfer mechanism in PFM is discussed and conditions for which linear imaging theory is applicable are determined. For these conditions, definitions for the Rayleigh two-point resolution, domain wall resolution, and information limit are formulated. For a Gaussian OTF, the *Rayleigh two-point resolution* is defined as $w_R = 1/q$ for which $F(q) = 0.58F(0)$. The experimentally accessible domain wall width is related to the Rayleigh defined resolution as $w_d = 0.626w_R$. Quantitative determination of material properties from a PFM image requires that characteristic domain sizes exceed w_R. OTF and RTR determined from diffractograms of periodic structures can be used to asses the fidelity of the writing process. Complementary RTR determined from the domain wall width determines the reading resolution. RTR defines the conditions under which the PFM can be used to study the intrinsic properties of the ferroelectric domain structures, including domain wall width and roughness. The information limit corresponds to the minimal feature size that can be measured experimentally and is defined by the condition $F(q) = N(q)$. Thus, the information limit defines the condition under which a domain is observable, but no reliable information about the local material properties or internal structure can be obtained. For PFM, the information limit can be significantly smaller than the RTR. Finally, the Rayleigh resolution in the PFM phase images is shown to be closely related to the information limit of their corresponding mixed signal images.

Experimental determination of the resolution function and subsequent reconstruction of an 'ideal image', reflecting the material properties and not the instrument properties, is demonstrated. Despite the fact that the resolution function in equation (4) is material specific, this approach can potentially be extended to image analysis in dissimilar materials if the dielectric properties and electric field distribution are known.

Acknowledgments

Support from ORNL SEED funding under contract DE-AC05-00OR22725 is acknowledged (SVK). Research sponsored by the Division of Materials Sciences and Engineering, Office of Basic Energy Sciences, US Department of Energy, under contract DE-AC05-00OR22725 with Oak Ridge National Laboratory, managed and operated by UT-Battelle, LLC.

References

[1] Gruverman A, Auciello O and Tokumoto H 1996 *J. Vac. Sci. Technol.* B **14** 602
[2] Gunther P and Dransfeld K 1992 *Appl. Phys. Lett.* **61** 1137
[3] Alexe M and Gruverman A (ed) 2004 *Nanoscale Characterization of Ferroelectric Materials* (Berlin: Springer)
[4] Hong S (ed) 2004 *Nanoscale Phenomena in Ferroelectric Thin Films* (Dordrecht: Kluwer)
[5] Roelofs A, Schneller T, Szot K and Waser R 2002 *Appl. Phys. Lett.* **81** 5231
[6] Ganpule C S, Nagarjan V, Li H, Ogale A S, Steinhauer D E, Aggarwal S, Williams E, Ramesh R and De Wolf P 2000 *Appl. Phys. Lett.* **77** 292
[7] Halperin C, Mutchnik S, Agronin A, Molotskii M, Urenski P, Salai M and Rosenman G 2004 *Nano Lett.* **4** 1253
[8] Kalinin S V, Rodriguez B J, Jesse S, Thundat T and Gruverman A 2005 *Appl. Phys. Lett.* **87** 053901
Kalinin S V, Rodriguez B J, Jesse S, Thundat T and Gruverman A 2005 *Preprint* cond-mat/0504232
[9] Tybell T, Paruch P, Giamarchi T and Triscone J-M 2002 *Phys. Rev. Lett.* **89** 097601
[10] Kalinin S V, Bonnell D A, Alvarez T, Lei X, Hu Z, Shao R and Ferris J H 2004 *Adv. Mater.* **16** 795
[11] Rodriguez B J, Nemanich R J, Kingon A, Gruverman A, Kalinin S V, Terabe K, Liu X Y and Kitamura K 2005 *Appl. Phys. Lett.* **86** 012906
[12] Abplanalp M, Zgonik M and Guenter P 2004 *Nanoscale Characterization of Ferroelectric Materials* ed M Alexe and A Gruverman (Berlin: Springer)
[13] Paruch P, Tybell T and Triscone J-M 2001 *Appl. Phys. Lett.* **79** 530
[14] Fujisawa H 2004 *Nanoscale Phenomena in Ferroelectric Thin Films* ed S Hong (Boston, MA: Kluwer–Academic)
[15] Nagarajan V and Ramesh R 2004 *Nanoscale Phenomena in Ferroelectric Thin Films* ed S Hong (Boston, MA: Kluwer–Academic)
[16] Paruch P, Giamarchi T, Tybell T and Triscone J-M 2004 *Preprint* cond-mat/0411178

[17] Cho Y 2004 *Nanoscale Characterization of Ferroelectric Materials* ed M Alexe and A Gruverman (Berlin: Springer)
[18] Cho Y, Hashimoto S, Odagawa N, Tanaka K and Hiranaga Y 2006 *Nanotechnology* **17** S137–41
[19] Kalinin S V, Karapetian E and Kachanov M 2004 *Phys. Rev.* B **70** 184101
[20] Karapetian E, Kachanov M and Kalinin S V 2005 *Phil. Mag.* **85** 1017
[21] Felten F, Schneider G A, Saldaña J M and Kalinin S V 2004 *J. Appl. Phys.* **96** 563
[22] Scrymgeour D A and Gopalan V 2005 *Phys. Rev.* B **72** 024103
[23] van Schendel P J A, Hug H J, Stiefel B, Martin S and Güntherodt H-J 2000 *J. Appl. Phys.* **88** 435
[24] Hug H J *et al* 1998 *J. Appl. Phys.* **83** 5609
[25] Jacobs H O, Leuchtmann P, Homan O J and Stemmer A 1998 *J. Appl. Phys.* **84** 1168
[26] Strassburg E, Boag A and Rosenwaks Y 2005 *Rev. Sci. Instrum.* **76** 083705
[27] Rayleigh L 1896 *Phil. Mag.* S **5** 167
[28] Fertig J and Rose H 1979 *Optik* **54** 165
[29] O'Keefe M A 1992 *Ultramicroscopy* **47** 282
[30] Sherzer O 1949 *J. Appl. Phys.* **20** 20
[31] Wade R H and Frank J 1977 *Optik* **38** 81
[32] Pennycook S J 2005 *Encyclopedia of Condensed Matter Physics* ed G Bassani, G Liedl and P Wyder (New York: Academic) pp 240–7
[33] Pennycook S J and Jesson D E 1990 *Phys. Rev. Lett.* **64** 938
[34] Nellist P D and Pennycook S J 1998 *Phys. Rev. Lett.* **81** 4156
[35] Nellist P D, Chisholm M F, Dellby N, Krivanek O L, Murfitt M F, Szilagyi Z S, Lupini A R, Borisevich A, Sides W H and Pennycook S J 2004 *Science* **305** 1741
[36] den Dekker A J 1997 *J. Opt. Soc. Am.* A **14** 547
[37] Villarrubia J S 1996 *J. Vac. Sci. Technol.* B **14** 1518
[38] Muller D J, Schabert F A, Buldt G and Engel A 1995 *Biophys. J.* **68** 1681
[39] Gutiérrez H R, Nakabayashi D, Silva P C, Bortoleto J R R, Rodrigues V, Clerici J H, Cotta M A and Ugarte D 2004 *Phys. Status Solidi* a **201** 888
[40] Meyer B and Vanderbilt D 2002 *Phys. Rev.* B **65** 104111
[41] Gull S F and Daniell G J 1978 *Nature* **272** 686
[42] McGibbon A J, Pennycook S J and Jesson D E 1999 *J. Microsc.-Oxford* **195** 44
[43] Puetter R C and Yahil A 1999 *Astronomical Data Analysis Software and Systems VIII* (*ASP Conf. Series* vol 172) ed D M Mehringer, R L Plante and D A Roberts (San Francisco, CA: ASP) pp 307–16
[44] Nellist P D and Pennycook S J 1998 *J. Microsc.-Oxford* **190** 159
[45] Shibata N, Pennycook S J, Gosnell T R, Painter G S, Shelton W A and Becher P F 2004 *Nature* **428** 730
[46] Molotskii M 2003 *J. Appl. Phys.* **93** 6234
[47] Morozovska A N and Eliseev E A 2006 *Phys. Rev.* **73** 104440
[48] Abplanalp M 2001 *Dr. Nat. Sci. Thesis* Swiss Federal Institute of Technology, Zurich
[49] Morozovska A N and Eliseev E A 2005 *Phys. Status Solidi* B **242** R79
[50] Kalinin S V, Gruverman A, Rodriguez B J, Shin J, Baddorf A P, Karapetian E and Kachanov M 2005 *J. Appl. Phys.* **97** 074305
[51] Emelyanov A Yu 2005 *Phys. Rev.* B **71** 132102
[52] Molotskii M and Shvebelman M 2004 *Ferroelectrics* **301** 67
[53] Triscone J M, private communications